Wide bandgap semiconductor conversion devices for radioisotope microbatteries

G. Lioliou,[1,a)] A.B. Krysa,[2] and A.M. Barnett[1]

[1] *Space Research Group, School of Mathematical and Physical Sciences, University of Sussex, Falmer, Brighton, BN1 9QT, UK*

[2] *EPSRC National Epitaxy Facility, University of Sheffield, Mappin Street, Sheffield S1 3JD, UK*

Abstract

Five mesa p^+-i-n^+ photodiodes (each of 0.126 mm^2 area) were investigated as conversion devices for X-ray-voltaics, in order to understand the comparative effects between different semiconductor materials, device structures, and X-ray incident power, and to explore them for use in future radioisotope microbatteries. Three semiconductor materials (AlInP, InGaP, and GaAs) and three i layer thicknesses of one material, AlInP (2 μm, 6 μm, and 10 μm), were investigated under the illumination of various controlled X-ray incident powers. The highest short circuit current was achieved with the GaAs device due to its thickest active layer and highest linear absorption coefficients at the most numerous incident X-ray photon energies (Mo Kα at 17.48 keV; Mo Kβ at 19.6 keV). The highest open circuit voltage was achieved with the 10 μm AlInP device due to its widest bandgap (cf. InGaP and GaAs) and its highest short circuit current (cf. the 2 μm and the 6 μm AlInP devices). The greatest output X-ray power was recorded with the InGaP device due to its highest fill factor (i.e. relatively low series and high shunt resistance) compared to the rest of the devices, although the GaAs device had the highest theoretical output X-ray power. A method for selecting the most suitable semiconductor material and device structure of conversion devices for radioisotope microbatteries (for exhibiting the highest power output) is presented considering the incident X-ray spectrum, while highlighting the importance of non-ideal device effects (reduced charge collection efficiency, increased series resistance, and reduced shunt resistance).

Keywords: X-ray-voltaics; radioisotope microbatteries; output power.

I. INTRODUCTION

Radioisotope microbatteries convert part of the energy emitted by a radioactive material and absorbed in the converter material into electrical energy. They consist of the radioactive material (e.g. a radioisotope X-ray, γ-ray, α particle, or β^- particle source), and the semiconductor conversion device. Radioisotope microbatteries are compact and offer high energy densities; the energy density of

[a)] Corresponding author. Tel.: +44 (0) 1273 872568. E-mail address: G.Lioliou@sussex.ac.uk

radioisotopes is 10^2 to 10^5 times higher than fossil fuels and chemical batteries [1]. This, along with their often long lifetimes, governed by the half-life of radioisotope sources used, can make radioisotope microbatteries an attractive power supply choice for applications where small amounts of power (typically at nW or μW levels) are required over long periods of time (tens of years). Radioisotope microbatteries are potentially high value power sources for Microelectromechanical Systems (MEMS) for biomedical [2], space and undersea exploration [3], as well as for security and defence applications [4].

The use of wide bandgap semiconductors for the conversion material of radioisotope microbatteries offers a variety of advantages compared to using Si. The energy conversion efficiency may be increased using a wide bandgap material [5]. Additionally, the low intrinsic carrier concentration of wide bandgap semiconductors enables their operation across a wider temperature range, compared to Si. The bandgap energies, E_g, of the semiconductors investigated here, $Al_{0.52}In_{0.48}P$, $In_{0.5}Ga_{0.5}P$, and GaAs are 2.31 eV [6], 1.9 eV [7], and 1.42 eV [7] at 300 K.

The voltaic effect induced in semiconductors by the absorption of photons, α particles, and β^- particles, which is the basic principle of operation of radioisotope microbatteries, has been investigated since the 1950s [8][9][10]. Recent studies on wide bandgap semiconductor conversion devices for radioisotope microbatteries have been conducted, including GaAs [11][12], $Al_{0.2}Ga_{0.8}As$ [13], $Al_{0.52}In_{0.48}P$ [14][15], $In_{0.5}Ga_{0.5}P$ [16], SiC [17][18], GaN [19] and diamond [20]. However, a direct comparison of the performance of previously reported radioisotope microbatteries in order to inform future radioisotope microbattery design cannot be made; the geometry of the semiconductor conversion devices and the incident radiation power differed. A comprehensive study to understand the comparative effects of the conversion device material and geometry, as well as that of the incident radiation power to the performance of the radioisotope microbatteries, is missing from the literature.

Here, five wide bandgap semiconductor devices (mesa p^+-i-n^+ photodiodes, each with an area of 0.126 mm^2) are investigated, in turn, as conversion devices for X-ray-voltaics, in order to understand the different contributions to their performance, compare the experimental results with the theory describing their operation, and draw conclusions to inform future radioisotope microbattery designs. The main aim of this work is to enhance understanding of the influence of the semiconductor material,

the device structure, and the incident radiation power on the performance of radioisotope microbatteries. For this reason, three different semiconductor materials, $Al_{0.52}In_{0.48}P$, $In_{0.5}Ga_{0.5}P$, and GaAs, and three different device thicknesses of the one material ($Al_{0.52}In_{0.48}P$), were investigated. In addition, the five semiconductor devices were subjected to the same, but varied, X-ray incident powers. This was achieved by using a Mo target X-ray tube as the incident radiation power and controlling the tube current. Various cell parameters are measured, and the results are analysed considering their performance as a function of semiconductor material, device thickness, and incident radiation power.

II. DEVICE STRUCTURE AND QUANTUM DETECTION EFFICIENCY

The semiconductor material and the structure of the devices investigated fulfilled two criteria: 1) the semiconductor material of the conversion device to have a wide bandgap, and 2) with the exception of the device thickness, all the other parameters of the devices (i.e. type of the structure, method for the structure growth, procedure for the device fabrication, area of the device, Ohmic contacts) to be identical in order to allow comparative studies. Five p^+-i-n^+ mesa structure conversion devices were investigated: three were $Al_{0.52}In_{0.48}P$ (herein after AlInP) each with a different i layer thickness; one was $In_{0.5}Ga_{0.5}P$ (InGaP); and one was GaAs. The layer structures of the devices are summarised in **Tables I**, **II**, and **III**. In each case, the material was grown by metalorganic vapour phase epitaxy (MOVPE) on a GaAs n^+ substrate.

Mesa structures were formed from the epi-wafers by wet chemical etching. For the 2 μm thick i layer AlInP device and the GaAs device, 1:1:1 H_3PO_4:H_2O_2:H_2O was used; 1:1:1 $K_2Cr_2O_7$:HBr:CH_3COOH was used for the 10 μm thick i layer AlInP device and the InGaP device. The etching of the 6 μm thick i layer AlInP device was started using 1:1:1 H_3PO_4:H_2O_2:H_2O, but due to the slow vertical etch rate achieved, it was then replaced by 1:1:1 $K_2Cr_2O_7$:HBr:CH_3COOH. Every device also received a 10 s finishing etch in 1:8:80 H_2SO_4:H_2O_2:H_2O. The intended diameter of the devices was 400 μm. Previous measurements of the diameter of a 6 μm thick i layer AlInP device fabricated using an identical fabrication process as for the 6 μm thick i layer AlInP device reported here, were performed using an optical microscope to investigate the potential effect of the fabrication process to its diameter [21]; the measurement suggested a diameter of 409 μm ± 28 μm, and it was thus

inconclusive as to whether the modified etching recipe used for the 6 μm thick i layer AlInP device affected its diameter. As such, all five devices were considered to have an area of 0.126 mm^2. On each device, a quasi-annular Ohmic top contact (20 nm Ti; 200 nm of Au) was formed which covered 33 % of the face of the device; planar 100 % coverage Ohmic contacts (20 nm InGe; 200 nm Au) were formed on the rear of the devices.

Table I. Layer details of the three AlInP p^+-i-n^+ mesa structures. The thickness of the nominally undoped i layer was 2 μm, 6 μm, and 10 μm.

Material	Type	Dopant	Thickness (μm)	Doping density (cm^{-3})
GaAs	p^+	Zn	0.01	1×10^{19}
AlInP	p^+	Zn	0.2	5×10^{17}
AlInP	i	-	2; 6; 10	Undoped
AlInP	n^+	Si	0.1	2×10^{18}
GaAs	n^+ (buffer)	Si	0.2	2×10^{18}
GaAs	n^+ (substrate)	Si	350	2×10^{18}

Table II. Layer details of the InGaP p^+-i-n^+ mesa structure.

Material	Type	Dopant	Thickness (μm)	Doping density (cm^{-3})
GaAs	p^+	Zn	0.01	1×10^{19}
InGaP	p^+	Zn	0.2	2×10^{18}
InGaP	i	-	5	Undoped
InGaP	n^+	Si	0.1	2×10^{18}
GaAs	n^+ (buffer)	Si	0.2	2×10^{18}
GaAs	n^+ (substrate)	Si	350	2×10^{18}

Table III. Layer details of the GaAs p^+-i-n^+ mesa structure.

Material	Type	Dopant	Thickness (μm)	Doping density (cm^{-3})
GaAs	p^+	C	0.5	2×10^{18}
GaAs	i	-	10	Undoped
GaAs	n^+	Si	1	2×10^{18}
GaAs	n^+ (substrate)	Si	350	2×10^{18}

The quantum detection efficiency, *QE*, of all five devices was calculated for photon energies from 1 keV to 35 keV, in accordance to the Beer-Lambert law; the results can be seen in **Fig. 1**. The quantum detection efficiency takes into account attenuation of X-rays at the inactive layers of the photodiodes (i.e. top Ohmic contact and top p^+ doped GaAs contact layer, assuming charge generated in this highly doped (1×10^{19} cm^{-3}) thin layer (0.01 μm) did not diffuse to the high-field active layer) and absorption of X-rays within the active layers of the photodiodes (i.e. p^+ and i layer) [22]. The X-ray linear attenuation and absorption coefficients of GaAs were extracted from Hubbell [23], whereas the linear absorption coefficients of AlInP and InGaP were calculated using the elemental (Al, In, P, and Ga) linear absorption coefficients [23] and the elements' appropriate weight fractions [24]. The linear absorption coefficients of AlInP, InGaP, and GaAs can be seen in **Fig. 1 (a)**. As an example, the linear absorption coefficient at 17.48 keV (Mo Kα) is 0.032 μm^{-1} for GaAs, 0.014 μm^{-1} for InGaP, and 0.007 μm^{-1} for AlInP.

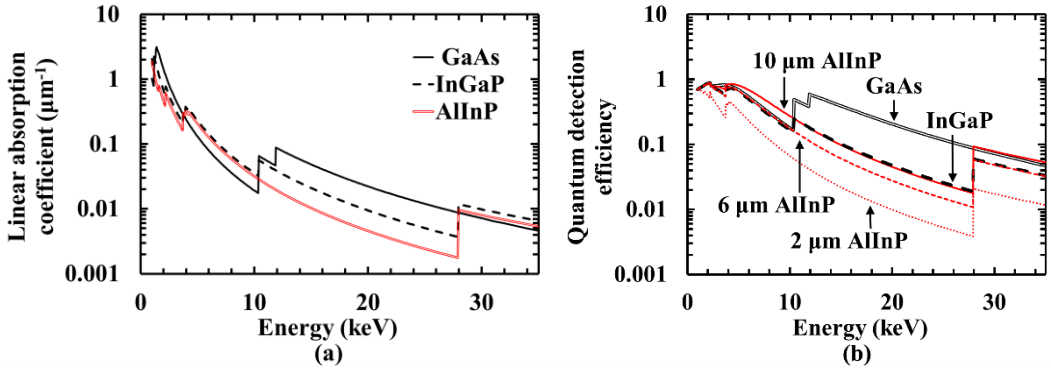

Figure 1. (a) Linear absorption coefficients for AlInP (red double solid line), InGaP (black dashed line), and GaAs (black solid line) and (b) quantum detection efficiency for the 2 μm AlInP (red round dotted line), 6 μm AlInP (red square dotted line), 10 μm AlInP (red solid line), InGaP (black dashed line), and GaAs (black double solid line) devices, as functions of X-ray photon energy.

Absorption edges, occurring at energies equal to the binding energies of the atoms of the devices, result in abrupt increases in linear absorption coefficient (and quantum detection efficiency). For example, the Ga K edge (10.367 keV), As K edge (11.867 keV), In K (27.940 keV) and L (3.730 keV) edges, and the P K edge (2.145 keV) can be seen in **Fig.1 (a)** [25]. The effect of increasing the i layer thickness (when everything else is kept the same) on the quantum detection efficiency can be seen in **Fig. 1 (b)** where the three thicknesses of i layer in the three AlInP structures (2 μm, 6 μm, and 10 μm)

are shown with their respective quantum detection efficiencies. As an example, the quantum detection efficiency at 17.48 keV (Mo Kα) is 0.015 for the 2 μm AlInP, 0.041 for the 6 μm AlInP, and 0.066 for the 10 μm AlInP devices.

III. CAPACITANCE MEASUREMENTS

The depletion width at 0 V applied bias and the effective carrier concertation of the intrinsic layer of each photodiode conversion device was determined from capacitance measurements. Measurement of both of these parameters gives a better insight into each of the conversion devices; the depletion width at 0 V partially defines the X-ray photo-generated current, I_L, and the effective carrier concentration within the i layer can be approximated to the concentration of the majority carriers in the intrinsic layer, with the former determining the depletion width at a given bias (see below). Each photodiode conversion device was mounted in an Al test fixture to provide dark conditions and electromagnetic shielding, and installed inside a Temperature Applied Sciences Micro LT225 environmental test chamber [26] for temperature control at 30 °C. The photodiodes were reverse biased using a Keithley 6487 Picoammeter/Voltage Source [27]. The capacitance was measured with a Hewlett-Packard 4275A Multi Frequency LCR meter [28]. The AC test signal of the LCR had an amplitude of 50 mV and a frequency of 1 MHz. Care was taken to separate the device capacitance from the package capacitance in each case; the capacitance measured between an empty pin (not wire bonded to a photodiode) adjacent to each photodiode and the common pin of the package was subtracted from the measured total packaged photodiode capacitance for each device. The uncertainty associated with the capacitance of each photodiode was estimated to be ± 0.1 pF.

The measured capacitance of each conversion device was used to calculate the depletion layer width, assuming that only the depletion layer capacitance accounted for the measured junction capacitance [29]; the calculated depletion layer widths of the five devices at 0 V applied bias are summarized in **Table IV**. The depletion width at no applied bias was found to be 1.94 μm ± 0.05 μm for the 2 μm AlInP, 0.89 μm ± 0.07 μm for the 6 μm AlInP, 1.2 μm ± 0.1 μm for the 10 μm AlInP, 4.2 μm ± 0.2 μm for the InGaP, and 9.3 μm ± 0.6 μm for the GaAs device. The uncertainties were determined by summating in quadrature the capacitance measurement uncertainties and the Debye

length as calculated for each semiconductor material at its corresponding carrier concentration (**Table IV**) [29]. As can be seen, none of the photodiodes were fully depleted at 0 V applied bias, but the 2 μm AlInP and the GaAs were almost fully depleted (97.0 % ± 2.5 %, and 93 % ± 6 %, respectively), assuming the devices had the intended epilayer thicknesses (i.e. these presented in **Tables I**, **II**, and **III**). The effective doping concentration of the intrinsic layer was extracted from the capacitance measurements using the differential capacitance method [29]; the results for the five devices at a distance below the p^+-i junction corresponding to the depletion width at 0 V applied bias are summarized in **Table IV**. The associated uncertainties of the effective carrier concentrations were related to the capacitance measurement uncertainties. The GaAs device had the lowest effective carrier concentration (3.6×10^{14} cm^{-3} ± 0.7×10^{14} cm^{-3}) within the i layer at a distance below the p^+-i junction corresponding to the depletion width at 0 V applied bias, whereas the rest of the devices had a value ~ 10^{15} cm^{-3}.

The effective carrier concentrations, N_{eff}, of the unintentionally doped i layers of the devices is an important parameter for their operation as conversion devices for radioisotope microbatteries. The ideal p^+-i-n^+ photodiode has a highly resistive i layer, which is fully depleted at 0 V applied bias [30], resulting in the maximum achievable *QE*, for a given device structure. However, the photodiodes reported here were not fully depleted at 0 V applied bias (**Table IV**) and thus their *QE* at 0 V applied bias and in photovoltaic mode is reduced compared to that at full depletion (shown in **Fig. 1**). The punch-through voltage,

$$V_{PT} = \frac{qN_{eff}W_i^2}{2\varepsilon_0\varepsilon}, \quad (1)$$

where q is the charge of an electron, W_i is the i layer thickness, ε_0 is the permittivity of free space, and ε is the relative permittivity of the semiconductor material, defines the required applied reverse bias for full depletion [30]. The punch-through voltage was calculated, given the extracted effective carrier concentration of each conversion device to be 10 V, 86 V, and 119 V for the 2 μm, the 6 μm, and the 10 μm AlInP device, respectively, 32 V for the InGaP device, and 25 V for the GaAs device. The lower the carrier concentration, N_{eff}, in the intrinsic layer, the lower the voltage required, V_{PT}, for full depletion,

for a given i layer thickness, W_i. Thus, a relatively low carrier concentration in the intrinsic layer would result in a wider depletion width at a given bias (in photovoltaic mode), compared to the depletion width for a relatively high carrier concentration at the same bias. As an example, if the effective carrier concentration within the i layer of the GaAs device decreased from 3.6×10^{14} cm^{-3} to 0.1×10^{14} cm^{-3}, the depletion width at 0 V would increase from 9.3 μm to 10 μm (full depletion), increasing its *QE* and the resultant photo-generated current.

IV. DARK AND X-RAY-VOLTAIC MEASUREMENTS

Dark and X-ray-voltaic measurements were performed for all five conversion devices. Each device was, in turn, positioned inside a custom Al test fixture, which was light tight, and which had a 4 μm thick Al X-ray window. A custom-made PTFE mount, kept at a fixed position, was used for accurate positioning of each device; the distance between the Al window and the top of each device was 14.5 mm. The test fixture was installed within a LD Didactic GmbH X-ray apparatus (part number 554 801) with a Mo target X-ray tube (part number 554 861) [31]. A custom-made Al collimator (90 mm in length), with internal PTFE lining thick enough to absorb completely all Al fluorescence X-rays from the collimator itself, and an aperture of 20 mm in diameter, collimated the X-rays from the X-ray tube. The Mo target X-ray tube was operated at selected potential differences up to 35.0 kV and selected tube currents up to 1.00 mA. The glass envelope of the X-ray tube was a high-borate borosilicate glass with a 1.4 mm thickness. The ambient temperature of the LD Didactic GmbH X-ray apparatus with the Mo target X-ray tube varied according to the X-ray tube current; it increased from ≈ 25 °C at 0.00 mA to ≈ 30 °C at 1.00 mA tube current. The total distance between the Mo target X-ray tube and the top of the X-ray-voltaic cells was 215 mm. The application of the conversion device bias and the measurement of the conversion device current (both dark and X-ray illuminated) was achieved using a Keithley 6487 Picoammeter/Voltage Source [27]. A schematic diagram of the experimental set up of the dark and X-ray-voltaic measurements can be seen in **Fig. 2**. Dry N_2 was continually flowing inside the Al test fixture to maintain an environment of low relative humidity (< 5 %) thus mitigating any humidity related effects on the photodiodes and the measured currents.

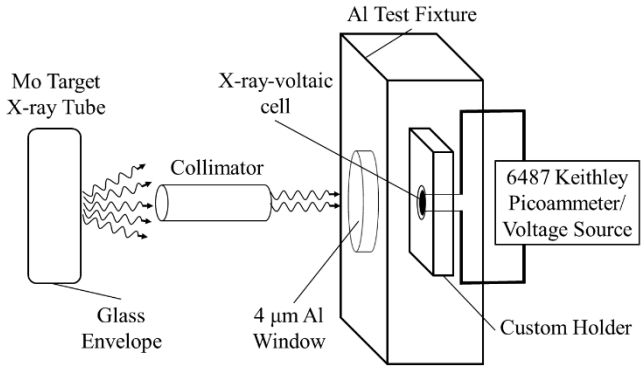

Figure 2. Diagram showing the experimental set up of the dark and X-ray-voltaic measurements.

The X-ray photon spectrum incident on the face of each X-ray-voltaic cell was predicted to aid an enhanced understanding of the comparative performance of the five conversion devices. Initially, the X-ray photon spectrum generated from the Mo target X-ray tube, at a potential difference of 35.0 keV, was predicted based on the Mo anode spectral model using interpolating polynomials [32]. The X-ray spectral model reported in Ref. [32] had a bin width of 0.5 keV and corresponded to a Mo target X-ray tube having a 0.5 mm Be window and no other filtration. Since the currently used Mo target X-ray tube did not have a Be window, the spectral model of Ref. [32] was adjusted accordingly to account for the absence of the Be window. The X-ray spectrum predicted to be generated by the Mo target X-ray tube was normalised to the maximum number of counts that occurred at 17.5 keV and can be seen in **Fig. 3**. It consisted of the characteristic Mo Kα and Mo Kβ X-rays [33] and a bremsstrahlung continuum. Then, the glass envelope of the X-ray tube (1.4 mm thick) was taken into account by considering its attenuation of the X-rays, and the resultant X-ray spectrum was calculated and can be seen in **Fig. 3**. As can be seen, the glass envelope greatly attenuated the low energy X-ray photons. Lastly, the attenuation of X-ray photons in the region between the X-ray tube and the top face of each X-ray-voltaic cell was calculated; here the X-ray photons were attenuated due to the air layer (200.5 mm thick) between the X-ray tube and the Al X-ray window of the test fixture (4 μm thick), and the N_2 layer (14.5 mm thick) between the Al window and the top of each X-ray-voltaic cell. The spectrum incident on each X-ray-voltaic cell, relative to the channel with the maximum number of counts (17.5 keV) in the predicted spectrum is shown in **Fig. 3**; the attenuation of X-rays between the outside envelope of the

X-ray tube and the top face of the X-ray-voltaic cells was negligible. The X-ray linear attenuation coefficients of Be, high-borate borosilicate glass, air, Al, and N_2 were all extracted from Hubbell [23].

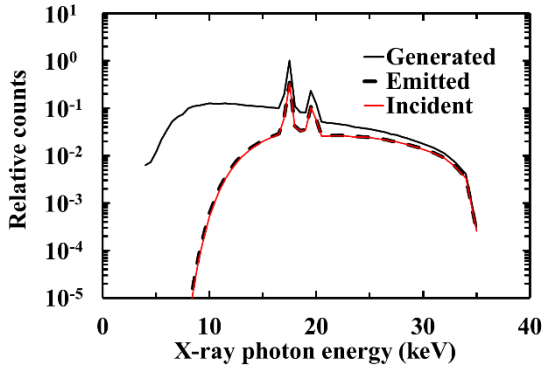

Figure 3. X-ray spectra generated by the X-ray tube (black solid line), emitted from the X-ray tube (black dashed line), and incident on the X-ray-voltaic cells (red solid line) relative to the height of the 17.5 keV peak in the X-ray spectrum generated by the X-ray tube.

Initially, the Mo target X-ray tube was unpowered; its current was set to 0.00 mA. Forward biased measurements with the conversion devices were made in 0.01 V increments, and the results can be seen in **Fig. 4**. The dark current increased with increasing applied forward bias. However, a different turn-on voltage was observed for different materials. The AlInP photodiodes had the highest turn-on voltage, whereas the GaAs photodiode, had the lowest turn-on voltage. This can be explained considering the proportionality of the turn-on voltage to the bandgap energy of the semiconductor material, similarly to the turn-on voltage increase with increasing bandgap reported for $In_{0.49}Ga_{0.51-x}Al_xP$ structures [34].

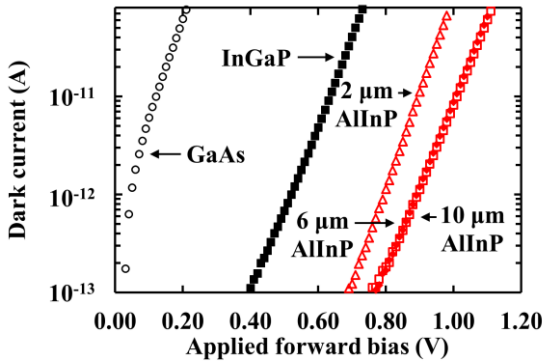

Figure 4. Dark current as a function of applied forward bias for all five photodiodes; 2 µm AlInP (red open triangle), 6 µm AlInP (red filled diamond), 10 µm AlInP (red open square), InGaP (black filled square), and GaAs (black open circle).

The ideality factor, n, and the saturation current, I_0, of the photodiodes were extracted from the forward biased current measurements [35]; a line of best fit was calculated, using linear least squares fitting, for the semi-logarithmic function of dark current as a function of forward bias (**Fig. 4**). The calculated ideality factor and saturation current values of all five photodiodes are summarized in **Table IV**. In general, ideality factor values close to 2 suggest that the recombination current dominates over the diffusion current [36]. The 2 μm AlInP device exhibited the lowest ideality factor; the value 1.694 ± 0.002 suggested that the forward current of this device was defined by both the recombination and the diffusion current. The GaAs device had the highest ideality factor (2.025 ± 0.002). The saturation current,

$$I_0 \propto \exp\left(\frac{-E_g}{nkT}\right), \tag{2}$$

where k is the Boltzmann constant and T is the temperature (in units of K), decreased exponentially with increasing bandgap energy, E_g. The AlInP devices (e.g. 1.61×10^{-20} A ± 0.01×10^{-20} A for the 2 μm AlInP device) had saturation currents three orders of magnitude lower than the InGaP device, with the latter having a saturation current five orders of magnitude lower than the GaAs device (3.78×10^{-12} A ± 0.01×10^{-12} A).

The X-ray tube was then switched on and the total current of each conversion device was measured. The X-ray tube potential difference was set to 35.0 kV throughout the measurements, and the tube current was varied from 0.10 mA to 1.00 mA, in 0.10 mA steps. The current as a function of applied forward bias was measured at each X-ray tube current, for all five conversion devices, and the results can be seen in **Fig. 5** for the InGaP device when illuminated with the X-ray tube at 1.00 mA.

The X-ray-voltaic response of a semiconductor p^+-i-n^+ photodiode is of the same nature as the photovoltaic response under illumination of photons of other energies (e.g. visible photons illuminating solar cells) albeit with differences in the charge creation processes at work upon absorption of the X-rays in the semiconductor. The X-rays absorbed in the conversion devices created electron-hole pairs. Compared to the processes of charge carrier creation in semiconductors in response to visible

wavelength photons, the processes of electron-hole pair creation in semiconductors in response to X-ray photons is more complex [37][38][39][40]. The movement of the charge carriers contributed to the photo-generated current, I_L [41]. At 0 V applied bias, and at moderate temperatures (including the temperatures experienced in this study, i.e. ≤ 30 °C), the photodiodes' dark currents were negligible; the measured total current, called the short-circuit current, I_{sc}, can be said to equal the X-ray photo-generated current [5],

$$I_{sc} = I_L, \text{ at 0 V}, \tag{3a}$$

and

$$I_L = \frac{E_{tot}}{\omega}\mathrm{q}, \tag{3b}$$

where ω is the electron-hole pair creation energy (see below) and E_{tot} (in units of eV s^{-1}) is the total useful X-ray energy absorbed per unit time which is dependent upon on the incident spectrum of illuminating radiation and the *QE* of each conversion device.

Another characteristic measure of the response of an X-ray-voltaic cell, and in general of conversion devices of microbatteries, is its open circuit voltage,

$$V_{oc} = \frac{n\mathrm{k}T}{\mathrm{q}}\ln\left(\frac{I_{sc}}{I_0} + 1\right) \approx \frac{n\mathrm{k}T}{\mathrm{q}}\ln\left(\frac{I_{sc}}{I_0}\right) \tag{4a}$$

and

$$\Delta V_{oc} = \frac{n\mathrm{k}T}{\mathrm{q}}\ln(\Delta P_{in}) \tag{4b}$$

where ΔV_{oc} is the difference in the open circuit voltage corresponding to a difference in incident power, ΔP_{in} [5]. The open circuit voltage is defined as the voltage at which the X-ray photo-generated current, I_L, equals (in magnitude) the diode's dark forward current, I_F, and since these two currents flow in opposite directions, the total current is zero. The theoretical maximum open circuit voltage equals the

bandgap voltage, E_g q^{-1}; the ratio between this theoretical maximum open circuit voltage and the measured V_{oc} is defined as the voltage efficiency, n_V.

A point of a particular interest on the current as a function of voltage curve of an X-ray-voltaic cell (e.g. **Fig. 5**) is the maximum power point; the voltage and the current corresponding to the maximum power point are V_m and I_m, respectively. The maximum power output of an X-ray-voltaic solar cell ($P_m = I_m V_m$) is always less than the power defined by the product of I_{sc} and V_{oc}; the ratio between the maximum power output, P_m, and the rectangle defined by the short circuit current, I_{sc}, and the open circuit voltage, V_{oc}, defines the fill factor,

$$F_F = \frac{I_m V_m}{I_{sc} V_{oc}} = \frac{P_m}{I_{sc} V_{oc}}. \quad (5)$$

The fill factor, F_F, measures the sharpness of the curve; the closer it is to 1, the higher the maximum output power will be [29]. The fill factor degrades due to parasitic (series and shunt) resistances of the photodiode [5]. More specifically: increase of the series resistance, R_S, may reduce the short circuit current, I_{sc}; reduction of the shunt resistance, R_{SH}, may reduce the open circuit voltage, V_{oc}; and either of these may reduce the fill factor, F_F.

Lastly, an important figure of merit for X-ray-voltaic cells is the power conversion efficiency, η, defined as the ratio between the maximum power output, P_m, and the incident power, P_{in},

$$\eta = \frac{P_m}{P_{in}} = \frac{I_{SC} V_{oc} F_F}{P_{in}}. \quad (6)$$

Hence, for a given incident power, P_{in}, the cell's power conversion efficiency is maximized when the short circuit current, I_{sc}, the open circuit voltage, V_{oc}, and the fill factor, F_F, are all maximized. It should be noted that the power conversion efficiency of an X-ray-voltaic cell usually decreases with increasing values of ideality factor, n, due to degradation of both V_{oc} and F_F [29].

Fig. 5 shows the dark and illuminated current as a function of applied forward voltage for the InGaP device, at an X-ray tube current of 1.00 mA; the open circuit voltage, V_{oc}, the short circuit current, I_{sc}, and the voltage, V_m, and the current, I_m, corresponding to the maximum power point, are also indicated.

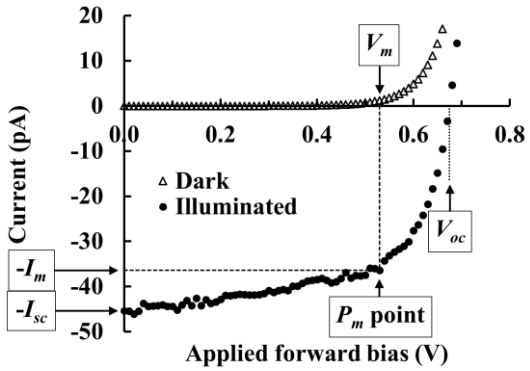

Figure 5. Dark (open triangles) and illuminated (filled circles) current as a function of applied forward bias, for the InGaP device, for an X-ray tube current of 1.00 mA. Also shown are the open circuit voltage, V_{oc}, and the short circuit current, I_{sc}, as well as the voltage, V_m, and current, I_m, corresponding to the maximum power, P_m, point. The uncertainty of the maximum output power point (omitted from the figure, for clarity) was necessarily related to the estimated uncertainties of determining V_m and I_m.

The short circuit current, I_{sc}, was measured for each device, as a function of X-ray tube current (X-ray incident power), and can be seen in **Fig. 6**; the short circuit current values achieved at the maximum X-ray tube current (1.00 mA) for each device are shown in **Table IV**. The short circuit current increased linearly with increasing X-ray tube current; a 10× increase in the incident X-ray power, from 0.10 mA to 1.00 mA X-ray tube current, resulted in an equal (10×) increase in the short circuit current, for all conversion devices. As an example, the ratio between the short circuit current at 1.00 mA and 0.10 mA X-ray tube current was 10.1 ± 0.2 for the GaAs conversion device.

In general, the short circuit current is affected by three processes. The first process is the useful X-ray photon absorption; usefully absorbed X-ray photons include those which were absorbed within the active region of the device as well as those absorbed within one carrier diffusion lengths from the active region. High absorption coefficients (**Fig. 1 (a)**), thick active regions, and long diffusion lengths all increase the useful X-ray photon absorption. Usefully absorbed X-ray photons lead to the creation of useful charge carriers; this is the second process that affects the short circuit current. Each X-ray photon absorbed, with an energy of E_{rad}, creates an average number of electron-hole pairs, N,

$$N = \frac{E_{rad}}{\omega} \quad (7)$$

where ω is the average energy consumed in the generation of an electron-hole pair (the parameter commonly termed the electron-hole pair creation energy). Thus, for an X-ray photon of a given energy, the lower the electron-hole pair creation energy, the greater the average number of generated charge carriers. The electron-hole pair creation energies of AlInP, InGaP, and GaAs at 30 °C are 5.31 eV [42], 4.96 eV [43], and 4.18 eV [44], respectively. Traditionally, the relationship between the electron-hole pair creation energy and bandgap energy was considered to be described by the Klein relationship [45][46] but recent results [47][48] have demonstrated the unsatisfactory nature of this model; carefully conducted measurements of modern high quality materials (Ge, Si, GaAs [44], $Al_{0.8}Ga_{0.2}As$ [47][48], $Al_{0.2}Ga_{0.8}As$ [49], $Al_{0.6}Ga_{0.4}As$ [50], $Al_{0.52}In_{0.48}P$ [42], and $In_{0.5}Ga_{0.5}P$ [43]) have revealed an alternative relationship, where $\omega = (1.54 \pm 0.07)\ E_g + (1.89 \pm 0.12)$ at 300 K for X-ray photons [50].

The movement of the created charge carriers under the effect of the internal electric field results in induced charge in the contacts of the photodiode, measured as photo-generated current, I_L. However, not all charge carriers generated give rise to as much photo-generated current as they might under ideal circumstances; incomplete charge collection, due to charge trapping and recombination, is the third process affecting the short circuit current, and may result in less photo-generated current compared to that which would be expected in the situation of 100 % charge collection efficiency. The charge collection efficiency is a function of the minority carrier lifetime; defect states (e.g. trapping and recombination centres) reduce the minority carrier lifetime which can in turn reduce the charge collection efficiency [51]. One cause of a reduction of minority carrier lifetime is radiation damage which can occur when semiconductor materials are exposed to radiation quanta of a particularly damaging nature (e.g. high-energy protons). The minority carrier lifetime, and thus the charge collection efficiency, greatly affects the operability and performance of a conversion device. The first and the third processes are very important, especially under forward bias, where the active region width and the internal electric field may be limited.

It should be added here, that the parasitic voltage drop due to series resistance of the photodiodes might reduce the measured short circuit current, I_{sc}. To summarize, the short circuit current is maximized by using an X-ray-voltaic cell made of a semiconductor material with high absorption coefficient at the X-ray energies of interest, long diffusion lengths, and low electron-hole pair creation energy. In terms of the device itself, high short circuit current is achieved for devices with thick active regions, high charge collection efficiencies, and negligible parasitic series resistance. As such, it can be seen that the short circuit current depends on a variety of cell parameters.

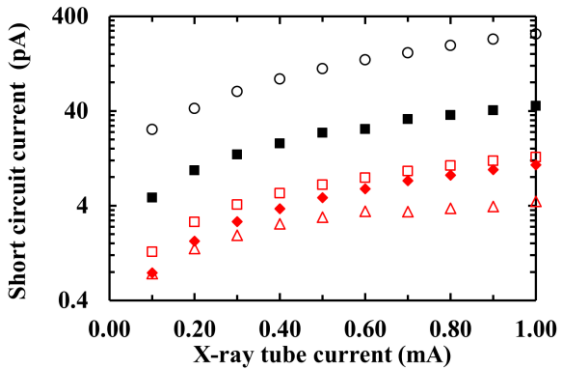

Figure 6. Short circuit current, I_{sc}, as a function of X-ray tube current for all five photodiodes; 2 μm AlInP (red open triangle), 6 μm AlInP (red filled diamond), 10 μm AlInP (red open square), InGaP (black filled square), and GaAs (black open circle).

The effect of the conversion device's charge collection efficiency and parasitic series resistance on the measured short circuit current of the three AlInP devices was investigated. The measured short circuit current per unit depletion width (at 0 V), $I_{sc}\ W_0^{-1}$, as a function of X-ray tube current, was calculated for the three AlInP conversion devices, and plotted in **Fig. 7**. It should be noted before proceeding further that whilst this measure ($I_{sc}\ W_0^{-1}$) is convenient and useful for present purposes, not all unit lengths of the depletion width contribute to the short circuit current equally, and as such, this measure is a mean value and does not necessarily relate to the specific contribution of any particular unit length. Conversion devices of the same semiconductor material have the same X-ray absorption coefficients, diffusion lengths, and electron-hole pair creation energy. Further normalising the measured short circuit current to unit depletion width, and comparing it among different conversion devices of the same semiconductor material (under the same X-ray spectrum of illuminating radiation)

highlights the effect of the charge collection efficiency and parasitic series resistance. The 6 μm AlInP and the 10 μm AlInP photodiodes showed a similar short circuit current per depletion width, 12 pA μm^{-1} for the 6 μm AlInP and 11 pA μm^{-1} for the 10 μm AlInP, whereas the 2 μm AlInP had only 2 pA μm^{-1}, at an X-ray tube current of 1.00 mA. This may be attributed to the 2 μm AlInP photodiode having a lower charge collection efficiency at 0 V and/or higher series resistance than the 6 μm AlInP and the 10 μm AlInP photodiodes. Previous X-ray spectra measurements using 2 μm AlInP devices fabricated from the same wafer as the 2 μm AlInP conversion device reported here suggested the presence of energy dependent incomplete charge collection noise arising from generated carrier trapping and/or recombination [52][53]; thus, set in context, the effect can be attributed to incomplete charge collection, at least in part. Subsequent X-ray spectra measurements using 6 μm AlInP devices showed that they did not exhibit signs of detectable incomplete charge collection noise under the illumination of X-ray photons of energy ≤ 21.17 keV [53]. Hence, the findings of **Fig. 7**, are in alignment with the previous results reporting lower charge collection efficiency of the 2 μm AlInP devices compared to 6 μm AlInP devices.

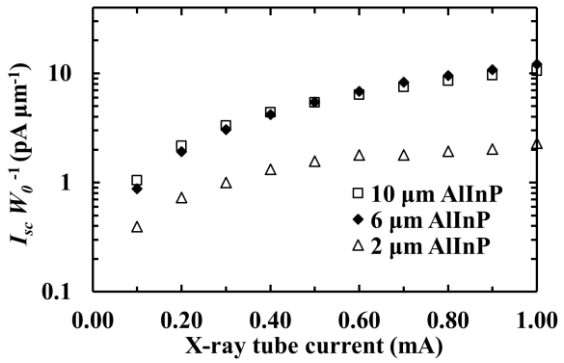

Figure 7. Measured short circuit current per depletion width, $I_{sc}\ W_0^{-1}$, as a function of X-ray tube current, for the three AlInP devices.

The total charge created from the X-ray energy absorbed per unit time, which resulted in the measured short circuit current, was calculated for all conversion devices at the maximum X-ray tube current, 1.00 mA, and can be seen in **Table IV**. This was done to emphasize the effect of the absorption coefficient and depletion layer width (i.e. *QE* of each X-ray-voltaic cell), the charge collection efficiencies, and the parasitic series resistance on the measured short circuit current of all five

conversion devices, excluding the effect of the electron-hole pair creation energy of each material. The useful energy absorbed, in eV s^{-1}, was calculated taking into account the measured short circuit current (in units of C s^{-1}) and the electron-hole pair creation energy (in units of eV) of each photodiode. The associated uncertainties resulted from the propagation of the measured short circuit current uncertainties (**Table IV**).

Amongst the investigated X-ray-voltaic cells, the GaAs photodiode had the highest short circuit current at each X-ray tube current (see **Fig. 6**). This was attributed to the device being almost fully depleted at 0 V (see **Table IV**), having the widest active layer thickness, the highest linear X-ray absorption coefficients within the energy range of interest (see below), and the lowest electron-hole pair creation energy. More charge carriers were generated for an absorbed X-ray photon of a given energy in the GaAs device compared to the rest of the devices. However, even when excluding the effect of the electron-hole pair creation energy of each photodiode, the GaAs device had the highest total useful X-ray energy absorbed per unit time (see **Table IV**). This was attributed to the GaAs having higher *QE* (wider active layer thickness and higher linear X-ray absorption coefficients) than the InGaP and AlInP devices within the energy ranges of 1.2 keV to 3.7 keV and 10.4 keV to 27.9 keV (see **Fig. 1**).

In order to verify the above, the effect of the different active layer thickness of each conversion device and the different X-ray absorption coefficients of each material on the short circuit current was considered, taking into account the specific X-ray spectrum of illuminating radiation. The X-ray spectrum incident on each X-ray-voltaic cell (**Fig. 3**) along with the *QE* of each X-ray-voltaic cell as a function of X-ray photon energy (assuming an active layer thickness equal to the depletion layer width at 0 V, **Table IV**) were combined to result in the calculated useful X-ray energy absorbed per unit time, in arbitrary units. Following this, the ratio between the measured (**Table IV**, at 1.00 mA X-ray tube current) and calculated X-ray energy usefully absorbed per unit time (in arbitrary units), was computed and can be seen in **Fig. 8**. This ratio highlights the effect of the charge collection efficiency and parasitic series resistance on the measured short circuit current, among all five conversion devices, since it is normalized to the active layer thickness and the X-ray absorption coefficients (through the *QE*), as well as the electron-hole pair creation energy. It can be seen that the 6 μm and the 10 μm AlInP had similar ratios, whereas the 2 μm AlInP exhibited a smaller ratio; both of these observations were in alignment

with the findings interpreted from **Fig. 7**. Another conclusion that can be drawn from **Fig. 8** is that the GaAs conversion device exhibited lower charge collection efficiency and/or higher parasitic series resistance than the 6 μm and the 10 μm AlInP device. Hence, the highest short circuit current measured with the GaAs conversion device could not be attributed to the device having relatively high charge collection efficiency and/or low parasitic series resistance, it was only attributed to the device having higher *QE* (wider active layer thickness and higher absorption coefficients) than the other devices at the energies of the most populous X-ray photons incident on the cells (Mo Kα at 17.48 keV and Mo Kβ at 19.6 keV). It should be noted here that only the depletion layer measured at 0 V was considered to contribute usefully to X-ray photon absorption; X-ray photon absorption within one diffusion length of the depletion layer was excluded (charge created in that region may have also contributed, by virtue of charge diffusion to the depletion layer).

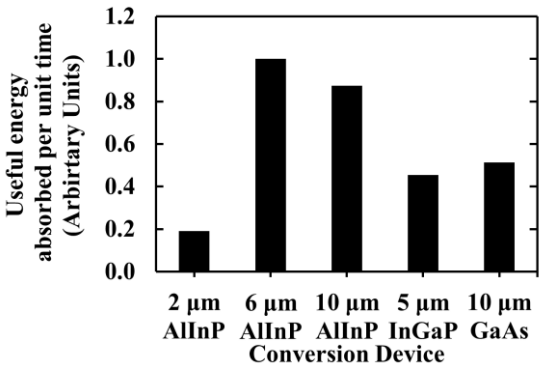

Figure 8. Ratio between measured and calculated X-ray energy usefully absorbed per unit time (in arbitrary units) for all five conversion devices.

Although the absolute value of the X-ray photon fluence incident on the conversion devices was not known (**Fig. 3**), its lower limit was calculated based on the measured useful X-ray energy absorbed per unit time with the 6 μm AlInP, which exhibited the highest ratio between the measured and calculated useful X-ray energy absorbed per unit time (**Fig. 8**). The X-ray photon fluence incident on the face of the conversion devices was found to be $\geq 2.7 \times 10^6$ photons mm^{-2}.

The influence of the specific X-ray spectrum of illuminating radiation on the short circuit current, I_{SC}, should not be disregarded. The number of X-ray photons and their corresponding energy plays an important role on the I_{SC}; the X-ray spectrum illuminating the currently reported X-ray-voltaic cells

mainly consisted of X-ray photons of energies 17.48 keV and 19.6 keV (**Fig. 3**). Thus, the semiconductor material with the highest linear absorption coefficients at these energies was advantageous (GaAs in this case, see **Fig. 1**). Another semiconductor could have been the material of choice for the X-ray-voltaic cell had the X-ray spectrum of illuminating radiation been different.

The open circuit voltage, V_{oc}, was measured for all X-ray-voltaic cells as a function of X-ray tube current; the results can be seen in **Fig. 9 (a)**. The open circuit voltage increased as the X-ray tube current (and hence, incident X-ray power) increased. This was in accordance with expectations since the open circuit voltage, V_{oc}, is logarithmically proportional to the short circuit current, I_{sc}, (**Eq. 4a**) and the short circuit current linearly increased with increasing X-ray tube current (**Fig. 6**). The open circuit voltage of all five photodiodes at 1.00 mA X-ray tube current can be seen in **Table IV**. According to **Eq. 4a**, the open circuit voltage, V_{oc}, is an increasing function of the short circuit current, I_{sc}, and a decreasing function of the saturation current, I_0. Thus, the open circuit voltage is maximized by maximizing I_{sc} (see discussion above) and maintaining low saturation current, I_0. A wide bandgap is advantageous for achieving a low saturation current (see **Table IV**) and thus, a high open circuit voltage, V_{oc}. The 10 μm and the 6 μm AlInP devices had the highest V_{oc}, the GaAs device had the lowest V_{oc}, whereas the InGaP device had a V_{oc} value between the highest and lowest, all in accordance with their bandgap energies, apart from the 2 μm AlInP device which is discussed in the following paragraph.

The AlInP conversion devices had similar saturation currents (**Table IV**) and thus it was expected that the device with the highest short circuit current would have the highest open circuit voltage (**Eq. 4a**). Indeed, the open circuit voltage at 1.00 mA (**Table IV**) of the AlInP conversion devices increased as the measured short circuit current at 1.00 mA (**Table IV**) increased. However, the differences in open circuit voltage of the AlInP conversion devices cannot be solely attributed to the different short circuit currents measured (**Fig. 6**). Possible different values of shunt resistance, R_{SH}, may have affected the open circuit voltage values measured. The theoretical open circuit voltage, V_{oc}, was calculated using **Eq. 4a**, and the measured values of I_0, n, and I_{sc}. The ratio between the measured and the theoretical V_{oc} at 1.00 mA X-ray tube current was calculated and the results suggested that the 2 μm AlInP device exhibited the lowest V_{oc}, cf. its theoretical value; the measured V_{oc} was 40 % of the theoretical value, whereas the InGaP device showed a measured V_{oc} of 96 % of its theoretical value. The limited measured

V_{oc} of the 2 μm AlInP was attributed to the device's reduced shunt resistance. Another observation based on **Fig. 9** is that, although the 6 μm AlInP had a greater open circuit voltage than that of the InGaP device, 0.770 V ± 0.005 V for 6 μm AlInP cf. 0.680 V ± 0.005 V for InGaP, the voltage efficiency, n_V, of the 6 μm AlInP (33 %) was lower than that of the InGaP device (36 %). The 10 μm AlInP device had the highest voltage efficiency (39 %).

A 10× increase in X-ray tube current, from 0.10 mA to 1.00 mA, resulted in a corresponding 10× increase in the incident X-ray power. The change in open circuit voltage, ΔV_{oc}, corresponding to a 10× increase in incident X-ray power, was measured (see **Fig. 9 (a)**) and was also calculated using **Eq. 4b**. A comparison between the measured and calculated change in V_{oc} corresponding to an increase of the X-ray tube current from 0.10 mA to 1.00 mA is presented in **Fig. 9 (b)**. The calculated increase in V_{oc} ranged from 0.10 V (for the 2 μm AlInP device) to 0.12 V (for the GaAs device), depending on the ideality factor of each conversion device. The percentage increase of the V_{oc} at 0.10 mA X-ray tube current, for a 10× increase in input X-ray power, was also calculated based on the measured V_{oc}. The biggest effect of the incident X-ray power increase to its open circuit voltage was recorded for the conversion device with the lowest V_{oc} at 0.10 mA, the GaAs device, which showed an increase of 110 % ± 10 %. This corresponded to a 2× increase of the GaAs device open circuit voltage for a 10× increase of the input X-ray power. In contrast, the 10 μm AlInP device showed the lowest percentage increase in V_{oc} as the X-ray tube current was increased to 1.00 mA, (12 % ± 5 %), since it had the highest value of V_{oc} at 0.10 mA X-ray tube current (0.81 V ± 0.4 V). These results highlight the weaker effect of the incident X-ray power increase to the open circuit voltage, compared to that of the short circuit current (see **Fig. 6**). However, it should be noted that the linear dependency of the short circuit current, I_{sc}, to the incident X-ray power does not provide any efficiency, η, improvement, since the P_{in} increases equally to I_{sc} (**Eq. 6**). It is this logarithmic dependency of the open circuit voltage on the short circuit current (and hence on the incident X-ray power, see **Eq. 4b**) that benefits the efficiency, η, and as has been seen, it mostly affects devices made from materials with narrow bandgap and thus relatively low open circuit voltage (e.g. GaAs in this case).

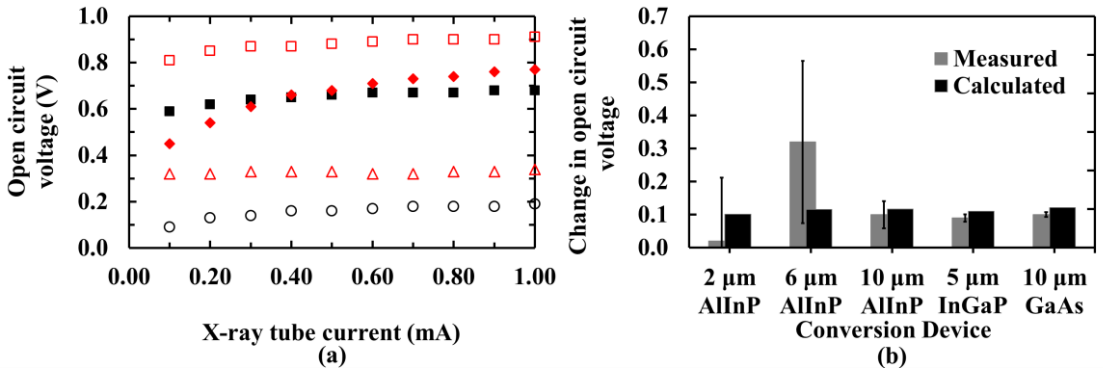

Figure 9. (a) Open circuit voltage, V_{oc}, as a function of X-ray tube current, measured for all five conversion devices; 2 µm AlInP (red open triangle), 6 µm AlInP (red filled diamond), 10 µm AlInP (red open square), InGaP (black filled square), and GaAs (black open circle) and (b) measured (grey) and calculated (black) change in open circuit voltage, ΔV_{oc}, for a change in incident X-ray power, ΔP_{in}, of 10× (i.e. from 0.10 mA to 1.00 mA X-ray tube current).

The fill factor, F_F, was then calculated using **Eq. 5** for all of the investigated X-ray-voltaic cells, at all investigated X-ray tube currents. It was found to be invariant (within uncertainties) with increasing X-ray power incident on the cell, within the investigated incident power increase (corresponding to an increase in X-ray tube current from 0.10 mA to 1.00 mA) for all devices apart from the GaAs device. The fill factor of the GaAs device increased from 0.25 ± 0.04 at 0.10 mA X-ray tube current to 0.36 ± 0.02 at 1.00 mA X-ray tube current. This was attributed to the fact that the fill factor is a function of the open circuit voltage, V_{oc}, [5] and that the V_{oc} of the GaAs device benefited a relatively greater amount from the increase in incident X-ray power cf. the rest of the devices (**Fig. 9 (a)**). The results of the fill factor at the maximum X-ray tube current (1.00 mA) can be seen in **Table IV**. The uncertainties were calculated based on the propagation of the uncertainties of the short circuit current, I_{SC}, the open circuit voltage, V_{OC}, and the voltage, V_m, and the current, I_m, corresponding to the maximum power point. The fill factor determines the power conversion efficiency of the X-ray-voltaic cell; it is maximized by minimizing the series and maximizing the shunt resistance of the photodiode [5]. The InGaP device had the highest fill factor among the investigated devices, whereas all the other photodiodes showed similar fill factor values. This may be attributed to the InGaP device having relatively low series resistance and relatively high shunt resistance. In conclusion, the fill factor of a conversion device for microbatteries is not directly affected by the semiconductor material or the device structure, as long as the device does not suffer from parasitic resistances. However, the fill factor of narrower bandgap materials benefits more from an increase in incident X-ray power, compared to the effect of the same

increase to devices made from wider bandgap materials. Lastly, it should be noted that increased incident X-ray power may increase the series resistance of the conversion device and consequently reduce its fill factor, something that was not observed in the reported devices up to the maximum investigated incident X-ray power (corresponding to an X-ray tube current of 1.00 mA).

The output power extracted from the reported X-ray-voltaic cells increased with increasing applied forward bias, up to a maximum value, P_m, corresponding to the current and voltage of I_m and V_m, respectively. The output power then decreased as the applied forward bias was increased beyond V_m. The maximum output power, P_m, was recorded for each X-ray-voltaic cell, and is presented in **Fig. 10** as a function of X-ray tube current. The maximum output power extracted from each X-ray-voltaic cell at 1.00 mA X-ray tube current can be seen in **Table IV**. The associated uncertainties resulted from the propagation and combination of the uncertainties in V_m and I_m.

The maximum output power, P_m, extracted from each X-ray-voltaic cell increased with increasing X-ray tube current (i.e. with increasing incident to the cell power, P_{in}). The ratio between the maximum output power measured at 1.00 mA X-ray tube current and that measured at 0.10 mA X-ray tube current, corresponding to a 10× increase in the incident X-ray power, was calculated. The highest value was calculated for the GaAs device, which exhibited (30 ± 4)× increase of its measured maximum output power for a 10× increase in the incident X-ray power. For comparison purposes, the InGaP conversion device showed a (13 ± 2)× increase of its maximum extracted power, when the X-ray tube current increased from 0.10 mA to 1.00 mA. The short circuit current, I_{sc}, increased linearly (**Fig. 6**) and the open circuit voltage, V_{oc}, increased logarithmically with incident X-ray power (**Fig. 9 (a)**). The benefit of the increased incident X-ray power to the open circuit voltage was relatively greater for the GaAs device, which had the lowest V_{oc} at 0.10 mA X-ray tube current, due to its narrowest bandgap c.f. the rest of the devices. Hence, the ratio between the maximum output power measured at 1.00 mA X-ray tube current and that measured at 0.10 mA X-ray tube current was the highest with the GaAs device due to it having the narrowest bandgap.

The highest maximum output power, P_m, was achieved with the InGaP X-ray-voltaic cell. Even though the GaAs device had the highest short circuit current, I_{sc}, and the 10 μm AlInP device had the highest open circuit voltage, V_{oc}, neither of these devices exhibited the highest maximum output power,

P_m. The P_m extracted from the InGaP device was mainly attributed to its highest fill factor, F_F (see **Eq. 6**). At the same time, the InGaP device had a moderate value (i.e. neither the highest nor the lowest) of I_{sc} and V_{oc} (see **Fig. 7** and **Fig. 9**) among the investigated X-ray-voltaic cells. This result highlights the importance of maximizing the cell parameters, I_{sc}, V_{oc}, and F_F (**Eq. 6**), to achieve high maximum output power. It also emphasizes the different trade-offs need to be taken into account when designing X-ray-voltaic cells.

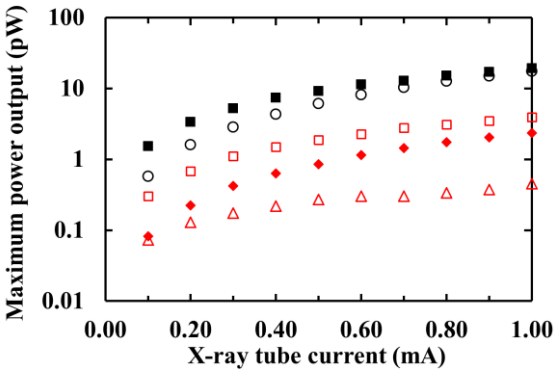

Figure 10. Maximum power output, P_m, as a function of Mo target X-ray tube current extracted from all X-ray-voltaic cells; 2 µm AlInP (red open triangle), 6 µm AlInP (red filled diamond), 10 µm AlInP (red open square), InGaP (black filled square), and GaAs (black open circle).

The maximum output power extracted from all X-ray-voltaic cells at 1.00 mA tube current was then normalised to the known conversion device parameters (linear X-ray absorption coefficients, active layer thickness, band gap energy, ideality factor, and electron-hole pair creation energy). This was done to investigate the achieved maximum output power with each conversion device excluding the effect of the X-ray spectrum of illuminating radiation as well as all the known conversion device parameters, to highlight the effect of the charge collection efficiency and parasitic series and shunt resistances to the achieved maximum output power.

Rearranging **Eq. 6**, and substituting I_{sc} from **Eq. 3a**, V_{oc} from **Eq. 4a** and I_0 from **Eq. 2**, it is found that

$$P_m \propto \frac{E_{tot}}{\omega} nkT \left(\ln\left(q \frac{E_{tot}}{\omega} \right) + \left(\frac{E_g}{nkT} \right) \right). \quad (8)$$

Hence, dividing the measured maximum output power of each conversion device, at 1.00 mA X-ray tube current, with the right hand side of **Eq. 8**, results in the comparison factor,

$$CF = \frac{P_m}{\frac{E_{tot}}{\omega} n\mathrm{k}T\left(\ln\left(\mathrm{q}\frac{E_{tot}}{\omega}\right)+\left(\frac{E_g}{nkT}\right)\right)} \tag{9}$$

which is a measure of the performance of the conversion devices for microbatteries, excluding known material related (linear X-ray absorption coefficients, band gap energy, and electron-hole pair creation energy) and device related (active layer thickness and ideality factor) parameters. The comparison factor was calculated for all five conversion devices and can be seen in **Table IV**. The associated uncertainties stated resulted from the propagation and combination of the uncertainties related to maximum output power, P_m, the active layer thickness (propagated through E_{tot}), and the ideality factor, n. The comparison factors, CF, of the 6 μm AlInP, the 10 μm AlInP, and the InGaP devices were the same within uncertainties. This suggested that the three conversion devices had comparable charge collection efficiencies and parasitic series and shunt resistances. The 2 μm AlInP had the lowest comparison factor among the investigated conversion devices. This was attributed to both the device's low charge collection efficiency and possible high series resistance (reducing its short circuit current and fill factor) as well as low shunt resistance (reducing its open circuit voltage and fill factor). The GaAs device had a comparison factor lower than the maximum achieved with the 6 μm AlInP, the 10 μm AlInP, and the InGaP devices, but higher than that achieved with the 2 μm AlInP device. Even though the GaAs device did not show signs of reduced shunt resistance, its short circuit current suggested the presence of non-negligible series resistance (**Fig. 8**). The maximum output powers of the 2 μm AlInP and GaAs devices were calculated assuming the devices showed comparable charge collection efficiencies and parasitic series and shunt resistances to the rest of the devices, considering the incident spectrum of illuminating radiation and the incident X-ray photon fluence ($\geq 2.7 \times 10^6$ photons mm^{-2}). This was found to be 7 pW for the 2 μm AlInP device and 34 pW for the GaAs device. In conclusion, the GaAs conversion device was found to exhibit the highest theoretical output power for the given incident X-ray spectrum of illuminating radiation, but the device's series resistance

reduced its output power (by reducing its short circuit current and fill factor) and thus, the InGaP conversion device exhibited the highest measured maximum output power.

Different cell design considerations need be taken into account in order to maximize the output power of an X-ray-voltaic conversion device. It has been shown that a wide bandgap and a low electron hole pair creation energy are both advantageous since they increase the achieved output power, but these two requirements represent design trade-off factors since they are conflicted. The X-ray spectrum of illuminating radiation also plays an important role in the selection of the semiconductor material for the cell; a material with high linear absorption coefficients at the X-ray photon energies of interest increases the achieved output power. The above analysis highlighted that the real-world device characteristics also greatly affect the performance of X-ray-voltaic cells. The engineer should aim for high quality devices: the effective carrier concentration of the unintentionally doped i layer should be kept as low as possible to allow thick depletion (active) layers at any given applied potential. Attention should also be given to the charge collection efficiency of the device, as well as to any parasitic series and shunt resistances, the combination of which may be catastrophic for the performance of an X-ray-voltaic cell, even if the material and device structure are otherwise optimized.

V. CONCLUSIONS

Five p^+-i-n^+ mesa structures (2 μm AlInP, 6 μm AlInP, 10 μm AlInP, InGaP, GaAs) have been investigated as conversion devices for radioisotope X-ray microbatteries; a comparative study of the effects of the semiconductor material, the device structure, and the incident radiation power on their performance was conducted in order to inform future radioisotope microbattery design.

Although none of the conversion devices were fully depleted at 0 V, the 2 μm AlInP device and the GaAs device were almost fully depleted in this condition (97.0 % ± 2.5 %, and 93 % ± 6 %, respectively). The effective carrier concentration of the GaAs i layer (3.6×10^{14} cm^{-3} ± 0.7×10^{14} cm^{-3}) was one order of magnitude lower than that of the rest of the devices, which resulted in the depletion region of the GaAs device at any given bias (in photovoltaic mode) being wider compared to those of the rest of the devices. This, along with the GaAs device having the greatest linear X-ray absorption coefficients at energies corresponding to the most populous incident X-ray photons, at 17.48 keV (Mo

Kα) and 19.6 keV (Mo Kβ), lead to the GaAs device benefiting from the highest *QE* at these energies amongst the devices.

The short circuit current increased linearly with increased X-ray tube current. The results suggested that the 2 μm AlInP device had poorer charge collection efficiency in photovoltaic mode and possibly higher series resistance cf. the 6 μm and 10 μm AlInP devices. The GaAs device exhibited the largest maximum I_{SC} (258 pA ± 1 pA).

The 10 μm AlInP conversion device had the highest maximum V_{oc} (0.91 V ± 0.01 V), due to this material having the widest bandgap energy amongst the materials characterised and the device having the greatest I_{SC} among the three AlInP devices. The 2 μm AlInP device exhibited the smallest V_{oc} relative to its theoretical value (40 %); this was attributed to its reduced shunt resistance. The InGaP device showed a measured V_{oc} which was 96 % of its theoretical value. An interesting observation was that the greatest effect of increasing the input X-ray power to the increase of V_{oc} (and fill factor) was observed with the conversion device which had the lowest V_{oc} at 0.10 mA (and the narrowest bandgap), i.e. the GaAs device.

The InGaP device had the largest fill factor (attributed to its relatively low series resistance and relatively high shunt resistance); all of the other photodiodes showed similar fill factor values. It was concluded that the fill factor of a device was not directly affected by the semiconductor material or the device structure, as long as the device did not suffer from parasitic resistances.

The maximum output power extracted from each X-ray-voltaic cell increased as the incident X-ray power was increased, with the GaAs device having the highest ratio between the maximum output power measured at 0.10 mA X-ray tube current and at 1.00 mA X-ray tube current (10× incident X-ray power increase). The InGaP device had the highest maximum output power (19.6 pW ± 0.3 pW); even though this device exhibited neither the highest short circuit current nor the highest open circuit voltage, it did have the greatest fill factor. Lastly, the calculated comparison factor (**Eq. 9**) suggested that: 1) the 6 μm AlInP, the 10 μm AlInP, and the InGaP devices had comparable charge collection efficiencies and parasitic (series and shunt) resistances, 2) the 2 μm AlInP device had lower charge collection efficiency and possibly higher series resistance (reducing its short circuit current and fill factor) and

lower shunt resistance (reducing its open circuit voltage and fill factor), and 3) the GaAs device had non-negligible series resistance (reducing its short circuit current and fill factor).

Although the GaAs device had the highest theoretical maximum output power, its series resistance reduced its achievable performance. In conclusion, knowledge of the radioisotope source spectrum of illuminating radiation can result in the selection of the most suitable semiconductor material and device structure when designing radioisotope microbatteries, but at the same time, the importance of growing high quality wafers and fabricating high quality devices should not be disregarded, as the real devices' non-ideal behaviours can greatly affect microbattery performance.

Table IV: For all five conversion devices, the following are shown: calculated depletion width at 0 V applied bias; calculated effective carrier concentration of the intrinsic layer at a distance below the p^+-i junction corresponding to the depletion width at 0 V applied bias; calculated ideality factor; calculated saturation current; measured short circuit current (at an X-ray tube current of 1.00 mA); measured total usefully absorbed X-ray energy per unit time (at an X-ray tube current of 1.00 mA); measured open circuit voltage (at an X-ray tube current of 1.00 mA); measured fill factor (at an X-ray tube current of 1.00 mA); extracted output power (at an X-ray tube current of 1.00 mA); and comparison factor (Eq. 9) (at an X-ray tube current of 1.00 mA).

Device	**Depletion width (μm)**	**Effective carrier concentration ($\times 10^{14}$ cm^{-3})**	**Ideality factor**	**Saturation current (A)**	**I_{SC} at 1.00 mA (pA)**	**Total useful X-ray energy absorbed ($\times 10^{7}$ eV s^{-1})**	**V_{OC} at 1.00 mA (V)**	**Fill factor**	**P_m at 1.00 mA (pW)**	***CF* (Eq. 9)**
2 μm AlInP	1.94 ± 0.05	31 ± 1	1.694 ± 0.002	1.61×10^{-20} $\pm 0.01 \times 10^{-20}$	4.4 ± 0.4	15 ± 1	0.34 ± 0.03	0.30 ± 0.08	0.6 ± 0.1	1.7 ± 0.4
6 μm AlInP	0.89 ± 0.07	29.6 ± 0.6	1.924 ± 0.003	2.03×10^{-20} $\pm 0.01 \times 10^{-20}$	10.7 ± 0.4	36 ± 1	0.77 ± 0.02	0.28 ± 0.03	2.4 ± 0.2	23 ± 3
10 μm AlInP	1.2 ± 0.1	14.8 ± 0.4	1.952 ± 0.006	2.53×10^{-20} $\pm 0.03 \times 10^{-20}$	13.0 ± 0.4	43 ± 1	0.910 ± 0.01	0.33 ± 0.03	3.9 ± 0.3	28 ± 2
5 μm InGaP	4.2 ± 0.2	17 ± 2	1.825 ± 0.007	1.74×10^{-17} $\pm 0.02 \times 10^{-17}$	45.4 ± 0.5	140 ± 2	0.680 ± 0.005	0.63 ± 0.01	19.6 ± 0.3	26.5 ± 0.5
10 μm GaAs	9.3 ± 0.6	3.6 ± 0.7	2.025 ± 0.002	3.78×10^{-12} $\pm 0.01 \times 10^{-12}$	258 ± 1	674 ± 3	0.190 ± 0.005	0.36 ± 0.02	17.4 ± 0.8	13.2 ± 0.6

ACKNOWLEDGEMENTS

This work was supported by the Science and Technology Facilities Council, United Kingdom, through grants ST/P001815/1, ST/R001804/1, and ST/T003391/1 and by the Engineering and Physical Sciences Research Council, United Kingdom, through grant EP/P021271/1 (University of Sussex, A.M.B., PI). A.M.B. acknowledges funding from The Leverhulme Trust, United Kingdom, in the form of a 2016 Philip Leverhulme Prize. The Authors acknowledge technical assistance from S. Butera, University of Sussex, UK, with some of the early measurements.

AUTHORS' DATA STATEMENT

All data that support the findings of this study are included within the article.

REFERENCES

[1] K.E. Bower, Y.A. Barbanel, Y.G. Shreter, and G.W. Bohnert, Polymers, Phosphors, and Voltaics for Radioisotope Microbatteries, CRC Press LLC, Boca Raton, 2002.

[2] E. Romero, R.O. Warrington, and M.R. Neuman, Physiological Measurement 30, R35 (2009).

[3] D. Qiao, X. Chen, Y. Ren, and W. Yuan, Journal of Microelectromechanical Systems 20, 685 (2011).

[4] P. Cabauy, L.C. Olsen, and N. Pan, Tritium direct conversion semiconductor device, Patent US8487507B1 (2009).

[5] A. Luque, and S. Hegedus, Handbook of Photovoltaic Science and Engineering, 2nd ed., John Wiley & Sons, Chichester, 2011.

[6] J.S. Cheong, J.S.L. Ong, J.S. Ng, A.B. Krysa and J.P.R. David, IEEE Journal of Selected Topics in Quantum Electronics 20, 142-146 (2014).

[7] I. Vurgaftman, J.R. Meyer and L.R. Ram-Mohan, Journal of Applied Physics 89, 5815 (2001).

[8] P. Rappaport, Physical Review 93, 246 (1954).

[9] J. Drahokoupil, M. Malkovská, and J. Tauc, Czechoslovak Journal of Physics 7, 57 (1957).

[10] K. Scharf, Journal of Research of the National Bureau of Standards-A. 64A, 297 (1960).

[11] H. Chen, L. Jiang, and X. Chen, Journal of Physics D: Applied Physics 44, 215303 (2011).

[12] S. Butera, G. Lioliou, and A.M. Barnett, Journal of Applied Physics 119, 064504 (2016).

[13] S. Butera, M.D.C. Whitaker, G. Lioliou, and A.M. Barnett, Scientific Reports 6, 38409 (2016).

[14] S. Butera, G. Lioliou, A.B. Krysa, and A.M. Barnett, Journal of Physics D: Applied Physics 49, 355601 (2016).

[15] S. Butera, M.D.C Whitaker, A.B. Krysa, and A.M. Barnett, Semiconductor Science and Technology 33, 105003 (2018).

[16] S. Butera, M.D.C. Whitaker, A.B. Krysa, and A.M. Barnett, Scientific Reports 7, 4981 (2017).

[17] C.J. Eiting, V. Krishnamoorthy, S. Rodgers, and T. George, Applied Physics Letters 88, 064101 (2006).

[18] M.V.S. Chandrashekhar, C.I. Thomas, H. Li, M.G. Spencer, and A. Lal, Applied Physics Letters 88, 033506 (2006).

[19] X. Tang, Y. Liu, D. Ding, and D. Chen, Science China Technological Sciences 55, 659 (2012).

[20] S.I. Maximenko, J.E. Moore, C.A. Affouda, and P.P. Jenkins, Scientific Reports 9, 10892 (2019).

[21] S. Zhao, S. Butera, G. Lioliou, A.B. Krysa, and A.M. Barnett, Scientific Reports 9, 12155 (2019).

[22] G.W. Fraser, X-ray Detectors in Astronomy, Cambridge University Press, Cambridge, 1989.

[23] J.H. Hubbell, The International Journal of Applied Radiation and Isotopes 33, 1269 (1982).

[24] R. Jenkins, R.W. Gould, and D. Gedcke, Quantitative X-Ray Spectrometry, 2nd ed., Marcel Dekker, New York, 1995.

[25] A. Thompson, D. Attwood, E. Gullikson, M. Howells, K.J. Kim, J. Kirz, J. Kortright, I. Lindau, Y. Liu, P. Pianetta, A. Robinson, J. Scofield, J. Underwood, G. Williams, and H. Winick, X-Ray Data Booklet (Center for X-Ray Optics and Advanced Light Source), Lawrence Berkeley National Laboratory, Berkeley, 2009.

[26] Temperature Applied Sciences Ltd, Goring Business Park, Goring-by-Sea, West Sussex, BN12 4HF, England, UK.

[27] Keithley Instruments, Model 6487 Picoammeter/Voltage Source Reference Manual, 6487-901-01 Rev C, Keithley Instruments, Ohio, 2011.

[28] Hewlett Packard, Model HP 4275A Multi-Frequency LCR Meter Operating Manual, 04275-90004, Hewlett Packard, Tokyo, 1979.

[29] S.M. Sze, and K.K. Ng, Physics of Semiconductor Devices, 3rd ed., John Wiley & Sons, New Jersey, 2007.

[30] J.F. White, Practical PIN Diodes, in Microwave Semiconductor Engineering, Springer, Dordrecht, 1982.

[31] LD Didactic GmbH, Instruction sheet, 554 800, LD Didactic GmbH, Huerth, 2014.

[32] J.M. Boone,T.R. Fewell, and R.J. Jennings, Medical Physics 24, 1863 (1997).

[33] M. Sánchez del Rio, A. Brunetti, B. Golosio, A. Somogyi, and A. Simionovici, A., XRAYLIB Tables (X-ray Fluorescence Cross-Section), European Synchrotron Radiation Facility and University of Sassari, 2003.

[34] J.P.R. David, M. Hopkinson, R. Ghin, and M.A. Pate, Proceedings of 1994 IEEE 6th International Conference on Indium Phosphide and Related Materials (IPRM), 403 (1994).

[35] G. Lioliou, X. Meng, J.S. Ng, and A.M. Barnett, Journal of Applied Physics 119, 124507 (2016).

[36] H. Spieler, Semiconductor Detector Systems, Oxford University Press, New York, 2005.

[37] G.W. Fraser, A.F. Abbey, A. Holland, K. McCarthy, A. Owens, and A. Wells, Nuclear Instruments and Methods in Physics Research Section A 350, 368 (1994).

[38] A. Owens, G.W. Fraser, A.F. Abbey, A. Holland, K. McCarthy, A. Keay, and A. Wells, Nuclear Instruments and Methods in Physics Research Section A 382, 503 (1996).

[39] F. Gao, L.W. Campbell, R. Devanathan, Y. Xie, L.R. Corrales, A.J. Peurrung, and W.J. Weber, Nuclear Instruments and Methods in Physics Research Section A 579, 292 (2007).

[40] F. Gao, L.W. Campbell, R. Devanathan, Y.L. Xie, Y. Zhang, A.J. Peurrung, and W.J. Weber, Nuclear Instruments and Methods in Physics Research Section B 255, 286 (2007).

[41] G.F. Knoll, Radiation Detection and Measurements, 4th ed., John Wiley & Sons, New Jersey, 2010.

[42] S. Butera, G. Lioliou, A.B. Krysa, and A.M. Barnett, Nuclear Instruments and Methods in Physics Research Section A 879, 64 (2018).

[43] S. Butera, G. Lioliou, A.B. Krysa, and A.M. Barnett, Nuclear Instruments and Methods in Physics Research Section A 908, 277 (2018).

[44] G. Bertuccio, and D. Maiocchi, Journal of Applied Physics 92, 1248 (2002).

[45] C.A. Klein, Journal of Applied Physics 39, 2029 (1968).

[46] A. Owens, and A. Peacock, Nuclear Instruments and Methods in Physics Research Section A 531, 18 (2004).

[47] A.M. Barnett, J.E. Lees, D.J. Bassford, and J.S. Ng, Journal of Instrumentation 7, P06016 (2012).

[48] A.M. Barnett, J.E. Lees, and D.J. Bassford, Applied Physics Letters 102, 181119 (2013).

[49] M.D.C. Whitaker, S. Butera, G. Lioliou, and A.M. Barnett, Journal of Applied Physics 122, 034501 (2017).

[50] M.D.C. Whitaker, G. Lioliou, A.B. Krysa and A.M. Barnett, Semiconductor Science and Technology 35, 095026 (2020).

[51] M.G. Spencer, and T. Alam, Applied Physics Reviews 6, 031305 (2019).

[52] G. Lioliou, S. Butera, A.B. Krysa, and A.M. Barnett, Nuclear Instruments and Methods in Physics Research Section A 943, 162467 (2019).

[53] S. Zhao, G. Lioliou, S. Butera, A.B. Krysa and A.M. Barnett, Nuclear Instruments and Methods in Physics Research Section A 960, 163606 (2020).